Shape-controlled nanoparticles in pore-confined space

Johannes Knossalla[b,†], Paul Paciok[c,†], Daniel Göhl[a], Daniel Jalalpoor[b], Enrico Pizzutilo[a], Andrea M. Mingers[a], Marc Heggen[c], Rafal E. Dunin-Borkowski[c], Karl J. J. Mayrhofer[a,d,e], and Ferdi Schüth[b,*], Marc Ledendecker[a,*]

[a] Department of Interface Chemistry and Surface Engineering, Max-Planck-Institut für Eisenforschung GmbH, Max-Planck-Strasse 1, 40237 Düsseldorf, Germany

[b] Department of Heterogeneous Catalysis, Max-Planck-Institut für Kohlenforschung, Kaiser-Wilhelm-Platz 1, 45470 Mülheim an der Ruhr, Germany

[c] Ernst-Ruska Centre for Microscopy and Spectroscopy with Electrons and Peter Grünberg Institute, Forschungszentrum Jülich, 52425 Jülich, Germany

[d] Forschungszentrum Jülich GmbH, Helmholtz Institute Erlangen-Nürnberg for Renewable Energy (IEK-11), Egerlandstr. 3, 91058 Erlangen, Germany

[e] Department of Chemical and Biological Engineering, Friedrich-Alexander-Universität Erlangen-Nürnberg, Egerlandstr. 3, 91058 Erlangen, Germany

†these authors contributed equally to this work.

a. Synthesis:

i. HGS synthesis via conventional wet-chemical methods

In previous publications, a detailed description of the synthesis of hollow graphitic spheres (HGS) can be found.[1,2] In principle, it consists of a nanocasting process by taking core shell mesoporous silica beads as the exotemplate, resulting in the carbon framework of the HGS.[3] The mesopores are filled sequentially via incipient wetness impregnation steps with $Fe(NO_3)_3$ solution (2M) and divinylbenzene. The HGS composite is obtained after carbonization, in which iron catalyses partial graphitization. Finally, after acid leaching of iron and silica, the HGS are obtained. In the following, the "/" symbol is used for the abbreviation of nanoparticles on the support such as e.g. "Pt/HGS".

ii. Pt_3Ni/C (octahedral):

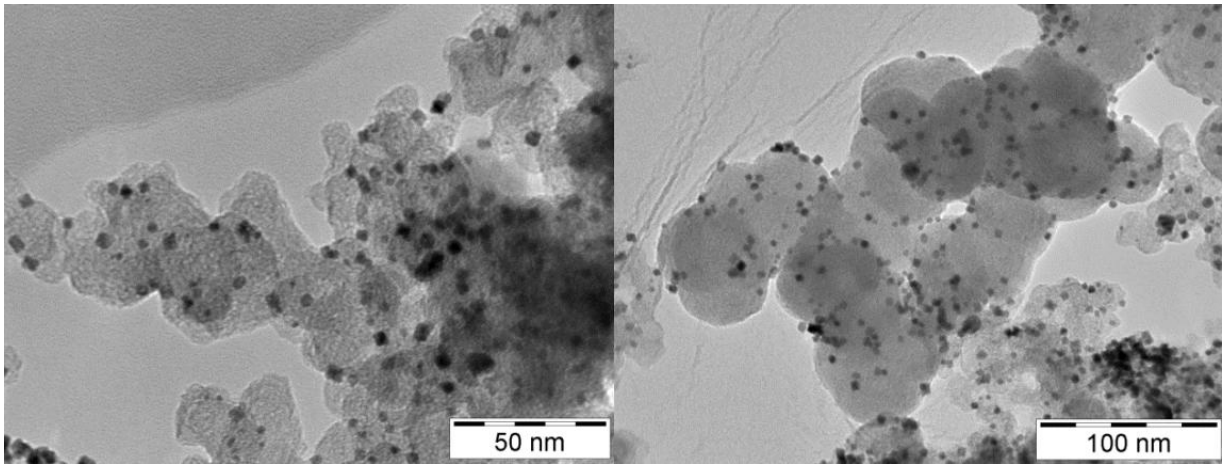

Figure S1: TEM micrographs of Pt_3Ni/C obtained through a solvothermal synthesis method at 160 °C in DMF and benzoic acid.

For the solvothermal synthesis, 80 mg of Vulcan® XC-72R (Cabot) is dispersed by sonication together with platinum(II) acetylacetonate (32 mg; 0.08 mmol; $Pt(acac)_2$; 95%; Sigma Aldrich), nickel(II) acetylacetonate (16 mg; 0.06 mmol; $Ni(acac)_2$; 97%; Sigma Aldrich), and benzoic acid (244 mg; 2 mmol; ≥99.5%; Sigma Aldrich) in dimethylformamide (40 ml; 99.8%; Sigma Aldrich) in a Teflon-inlet (50 ml). The inlet is placed in a steel-autoclave that is heated to 160 °C for 12 h. The samples are collected by centrifugation (16500 rpm; 5 min) and washed subsequently three times with acetone/ethanol (1:1) and three times with chloroform. Finally, the samples are dried at 50 °C for 12 h.

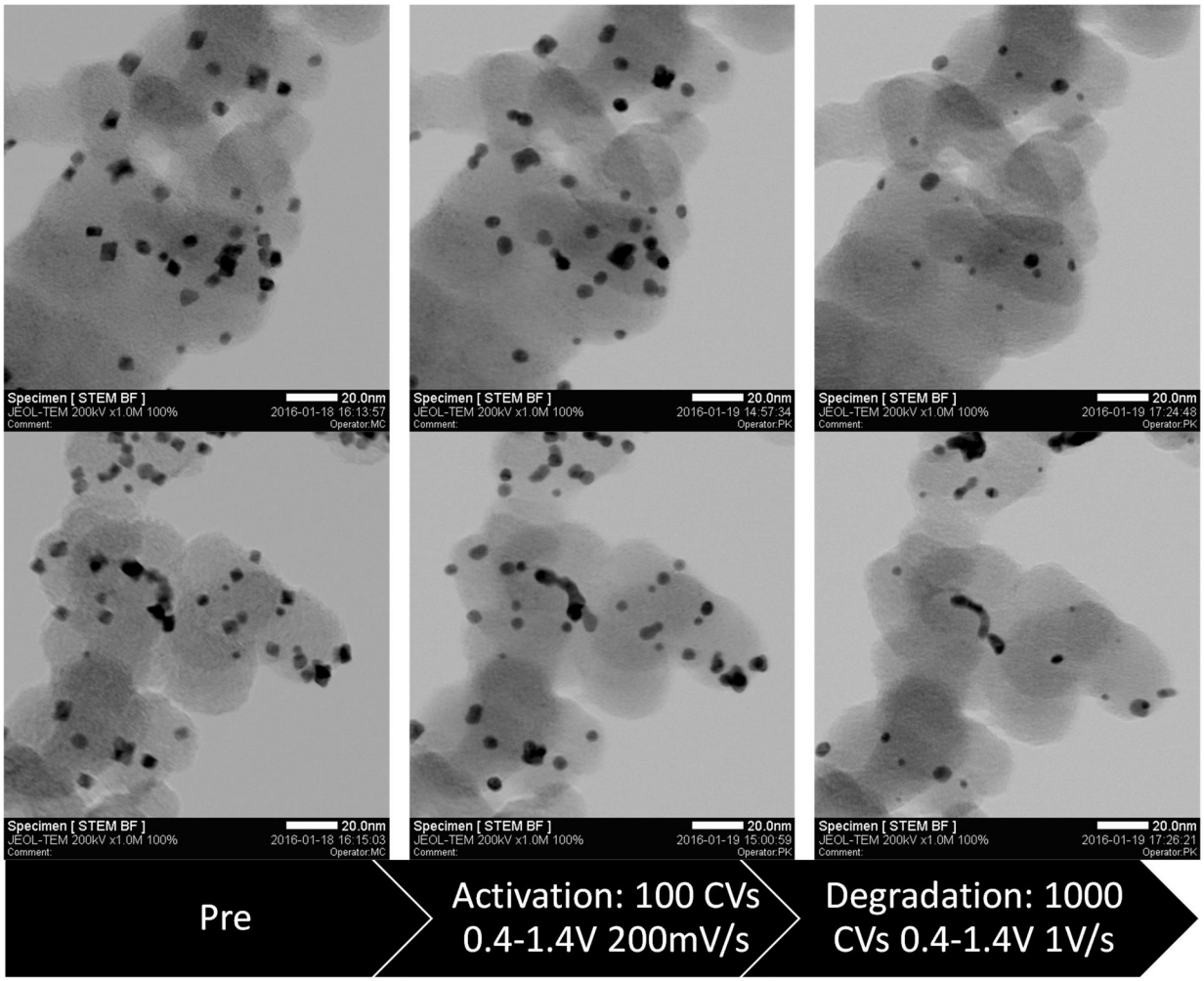

Figure S2: IL-TEM images of Pt_3Ni /C before (top) and after 200 and 1000 potential cycling (bottom) between 0.4 and 1.4 V vs. RHE; 1 V s^{-1} in 0.1M $HClO_4$.

iii. Pt_3Ni-Mo/C (octahedral):

For the solvothermal synthesis, 80 mg of Vulcan® XC-72R (Cabot) is dispersed by sonication together with platinum(II)acetylacetonate (8 mg; 0.02 mmol; $Pt(acac)_2$; 95%; Sigma Aldrich), nickel(II) acetylacetonate (4 mg; 0.016 mmol; $Ni(acac)_2$; 97%; Sigma Aldrich), and molybdenumhexacarbonyl (1.6 mg; 0.006 mmol; $Mo(CO)_6$; 98%; Sigma Aldrich) are added to the suspension, which is in the following sonicated for 10 min, sealed, and placed in the steel-autoclave. The solvothermal process is conducted by heating to 170 °C for 45 h. The samples are collected by centrifugation (16500 rpm; 5 min) and washed subsequently three times with acetone/ethanol (1:1) and three times with chloroform. Finally, the samples are dried at 50 °C for 12 h.

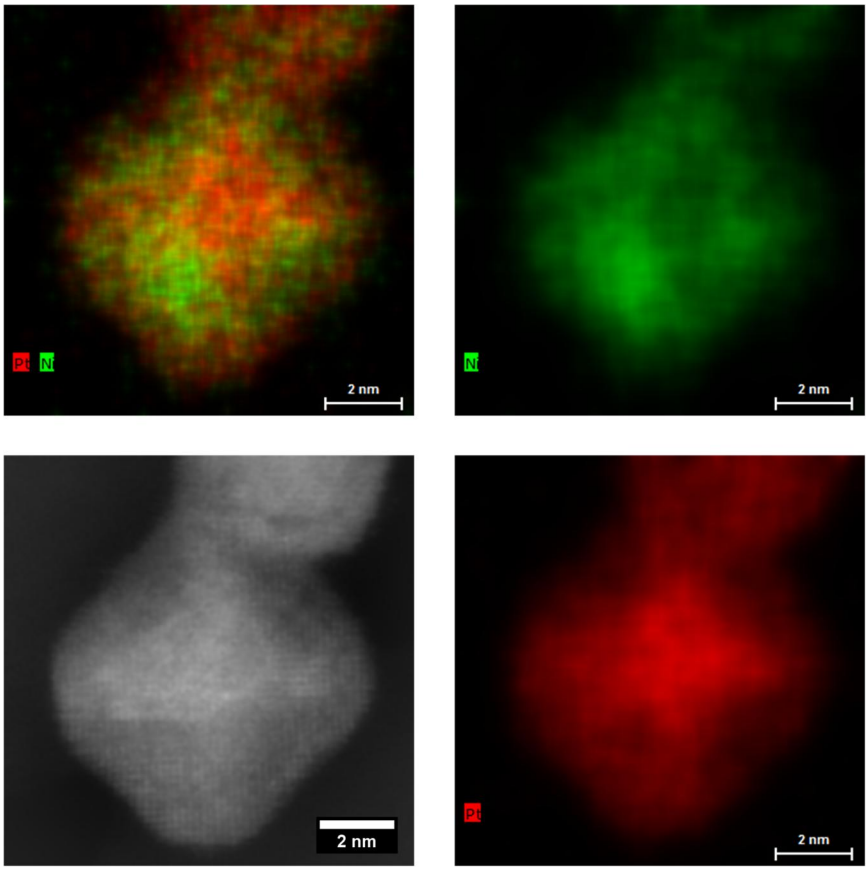

Figure S3: HAADF STEM micrographs of Pt_3Ni-Mo/C and the corresponding EDX mapping of the elements Pt and Ni.

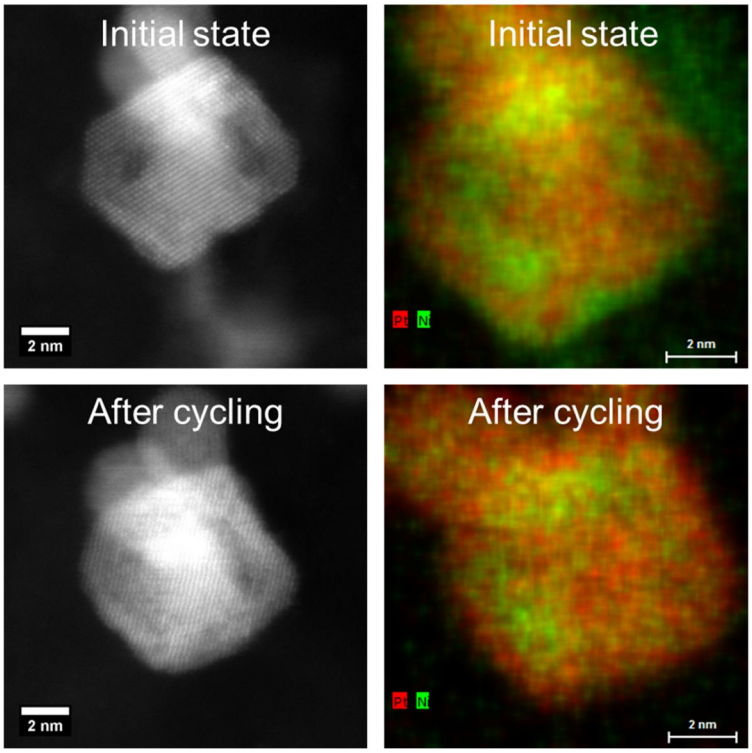

Figure S4: IL-STEM HAADF images and corresponding Pt/Ni elemental maps of Pt_3Ni-Mo/C before (top) and after 10800 potential cycling (bottom) between 0.4 and 1 V vs. RHE; 1 V s^{-1} in 0.1M $HClO_4$.

iv. Pt_3Ni/HGS (outside of pores):

For the solvothermal synthesis, 80 mg of HGS is dispersed by sonication together with platinum(II) acetylacetonate (32 mg; 0.08 mmol; $Pt(acac)_2$; 95%; Sigma Aldrich), nickel(II) acetylacetonate (16 mg; 0.06 mmol; $Ni(acac)_2$; 97%; Sigma Aldrich), and benzoic acid (244 mg; 2 mmol; ≥99.5%; Sigma Aldrich) in dimethylformamide (40 ml; 99.8%; Sigma Aldrich) in a Teflon-inlet (50 ml). The inlet is placed in a steel-autoclave that is heated to 160 °C for 12 h. The samples are collected by centrifugation (16500 rpm; 5 min) and washed subsequently three times with acetone/ethanol (1:1) and three times with chloroform. Finally, the samples are dried at 50 °C for 12 h.

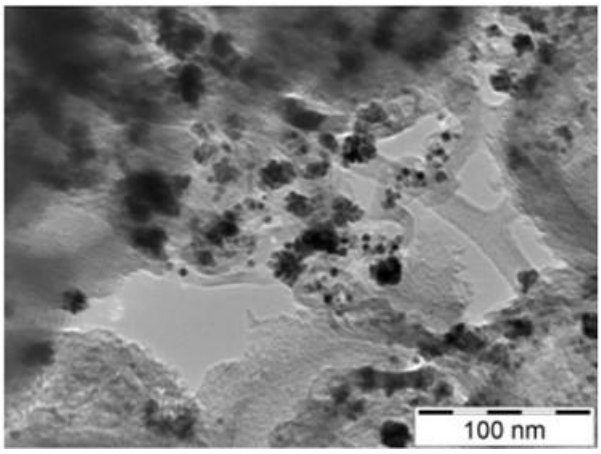

Figure S5: TEM micrographs of Pt_3Ni/HGS where no seed particles have been used. The results are low particle dispersion and a high degree of agglomeration.

v. Pt_3Ni-Mo/HGS (outside of pores)

For the solvothermal synthesis, 80 mg of HGS is dispersed by sonication together with platinum(II)acetylacetonate (8 mg; 0.02 mmol; $Pt(acac)_2$; 95%; Sigma Aldrich), nickel(II) acetylacetonate (4 mg; 0.016 mmol; $Ni(acac)_2$; 97%; Sigma Aldrich), and molybdenumhexacarbonyl (1.6 mg; 0.006 mmol; $Mo(CO)_6$; 98%; Sigma Aldrich) are added to the suspension, which is in the following sonicated for 10 min, sealed, and placed in the steel-autoclave. The solvothermal process is conducted by heating to 170 °C for 45 h. The samples are collected by centrifugation (16500 rpm; 5 min) and washed subsequently three times with acetone/ethanol (1:1) and three times with chloroform. Finally, the samples are dried at 50 °C for 12 h.

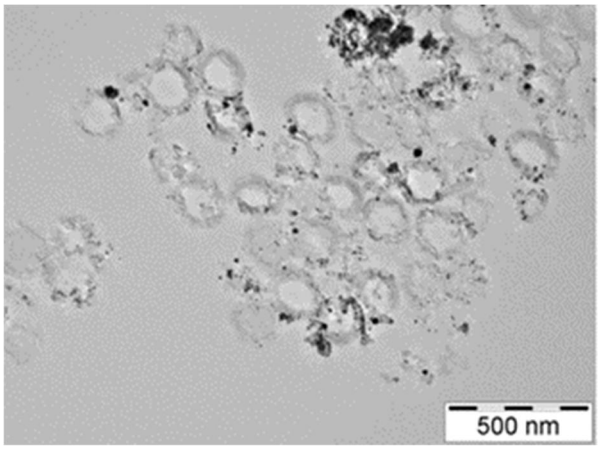

Figure S6: TEM micrographs of Pt_3Ni-Mo/HGS where no seed particles have been used. The results are low particle dispersion and a high degree of agglomeration similar to Pt_3Ni/HGS.

vi. Pt_{seed}/HGS (inside pores)

First, Pt metal precursors are impregnated via incipient wetness impregnation. For a typical synthesis of 100 mg Pt/HGS (2wt% metal), 98 mg of the HGS support are impregnated with an aqueous solution of the corresponding metal precursors. $H_2PtCl_6*xH_2O_{aq}$ (0.096 ml; 1.07 mol/L; ≥99.9%; Sigma Aldrich) and Millipore water (0.018 ml; 18.2 MΩ cm at 25 °C) is added, correlating to the total pore volume (1.0–1.3 cm^3/g) of the employed sample. In order to ensure pore filling, the powder is sonicated for 30 min. In the second step, the sample is dried, followed by a reduction with hydrogen. The powder is transferred in a crucible boat and placed in a tube furnace. Drying is ensured by 30 min at 120 °C (heating rate: 3°K/min) under argon flow (300 ml/min). Reduction of the metal precursors is performed at 220 °C and a H_2/Ar gas mixture (300 ml/min; 15vol% H_2) for 1.5 h. After the reduction step, the H_2 gas flow is turned off and the oven is left to naturally cool down to ambient temperature.

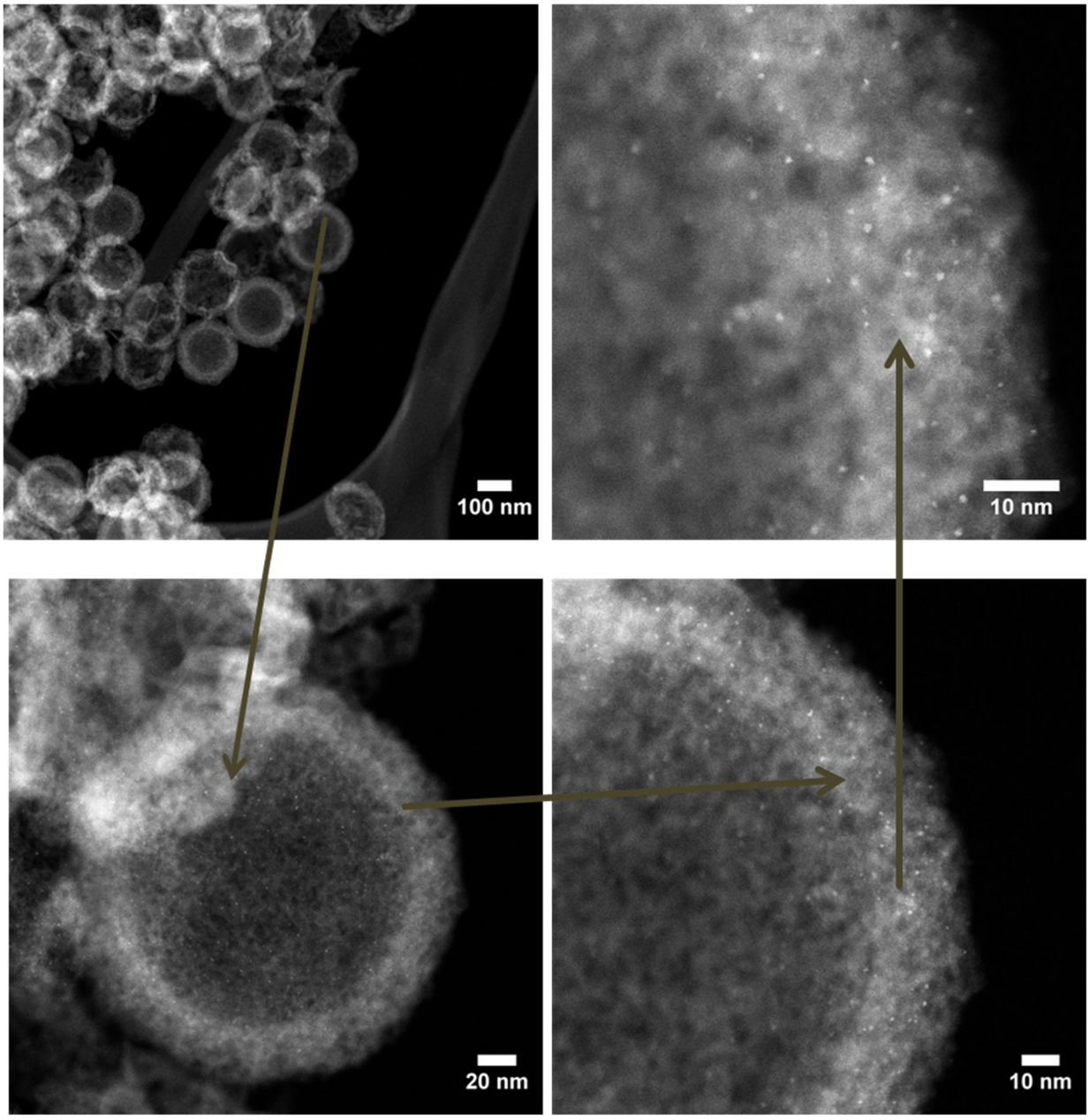

Figure S7: Pt_{seed} particles incorporated into the HGS material after Incipient wetness impregnation and reduction.

vii. Pt_{seed}/Pt_3Ni/HGS (octahedral, inside pores)

For the synthesis, Pt_{seed}/HGS (2wt%) is employed as starting material. The Pt_{seed}/HGS precursor is obtained following the incipient wetness impregnation protocol and subsequent reduction, as described above. The seed concentration predefines the final metal loading and is key, together with the added metal concentration, for the synthesis of high aspect-ratio nanomaterials. Taking into account the volume increase during the last overgrowth process, an initial Pt seed loading of 2wt% was chosen, resulting in a final metal loading of 30 wt%. For the solvothermal synthesis the corresponding carbon support (80 mg; Pt_{seed}/HGS) is dispersed by sonication together with platinum(II) acetylacetonate (32 mg; 0.08 mmol; $Pt(acac)_2$; 95%; Sigma Aldrich), nickel(II) acetylacetonate (16 mg; 0.06 mmol; $Ni(acac)_2$; 97%; Sigma Aldrich), and benzoic acid (244 mg; 2 mmol; ≥99.5%; Sigma Aldrich) in dimethylformamide (40 ml; 99.8%; Sigma Aldrich) in a Teflon-inlet (50 ml). The inlet is placed in a steel-autoclave that is heated to 160 °C for 12 h. The samples are collected by centrifugation (16500 rpm; 5 min) and washed subsequently three times with acetone/ethanol (1:1) and three times with chloroform. Finally, the samples are dried at 50 °C for 12 h.

Calculations to determine the ratio between initial loading with spherical particles and final loading with octahedral particles:

$$V_{sphere} = \frac{1}{6}\pi d^3 = \frac{1}{6}\pi 1{,}5^3 = 1{,}77\ nm^3$$

$$V_{Oktaeder} = \frac{a^3}{3}\sqrt{2} = \frac{4.2^3}{3}\sqrt{2} = 34.93\ nm^3$$

$$V_{Shell} = V_{Oktaeder} - V_{Sphere} = 33.16\ nm^3$$

$$\varphi_{Shell,Ni} = \frac{V_{Ni}}{V_{Ni} + V_{Pt}} = \frac{\frac{0.9\ mg}{8.908\ {}^{g}/_{cm^3}}}{\frac{0.9\ mg}{8.908\ {}^{g}/_{cm^3}} + \frac{4\ mg}{21.45\ {}^{g}/_{cm^3}}} = 36\%$$

(Proportion based on the synthesis protocol of X. Huang, Z. Zhao, L. Cao, Y. Chen, E. Zhu, Z. Lin, M. Li, A. Yan, A. Zettl and Y. M. Wang, Science, 2015, 348, 1230-1234.)

$$V_{Shell} * \varphi_{Shell} = V_{Shell,Ni} = 11.8\ nm^3$$

$$V_{Shell,Pt} = 21.3\ nm^3$$

$$f = \frac{m_{Sphere}}{m_{Shell}} = \underline{14.9}$$

viii. Pt_{seed}/Pt_3Ni-Mo/HGS (octahedral, inside pores)

For the synthesis, Pt_{seed}/HGS (2wt%) is employed as starting material. The Pt_{seed}/HGS precursor is obtained following the incipient wetness impregnation protocol and subsequent reduction as described above.

After the synthesis of Pt_{seed}/HGS, platinum(II) acetylacetonate (8 mg; 0.02 mmol; $Pt(acac)_2$; 95%; Sigma Aldirch), nickel(II) acetylacetonate (4 mg; 0.016 mmol; $Ni(acac)_2$; 97%; Sigma Aldrich), and molybdenumhexacarbonyl (1.6 mg; 0.006 mmol; $Mo(CO)_6$; 98%; Sigma Aldrich) are added to the suspension of Pt_{seed}/HGS in benzoic acid and DMF, which is in the following sonicated for 10 min, sealed, and placed in the steel-autoclave. The volume of the Pt/Ni solution was chosen to be equal to the pore volume obtained from BET analysis. The solvothermal process is conducted by heating to 170 °C for 45 h. Samples are obtained by centrifugation (16500 rpm; 5 min) and washed subsequently three times with acetone/ethanol (1:1) and three times with chloroform. Finally, the samples are dried at 50 °C for 12 h.

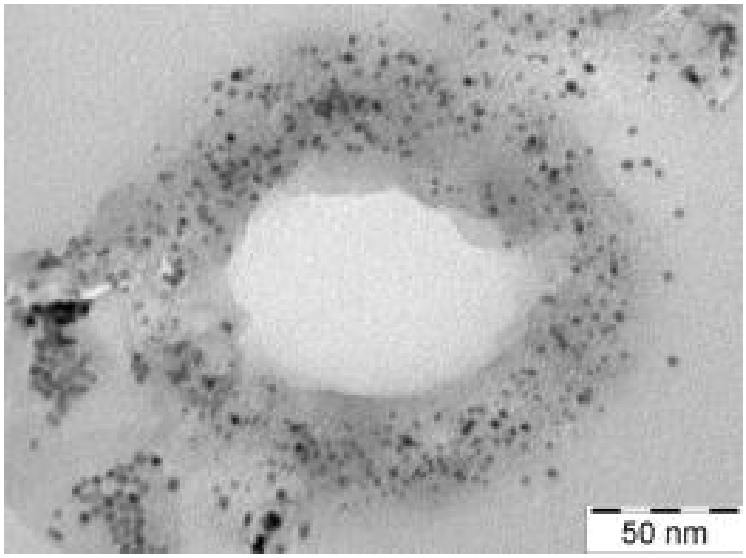

Figure S8: Cross-sectional TEM micrographs of Pt_{seed}/Pt_3Ni-Mo/HGS.

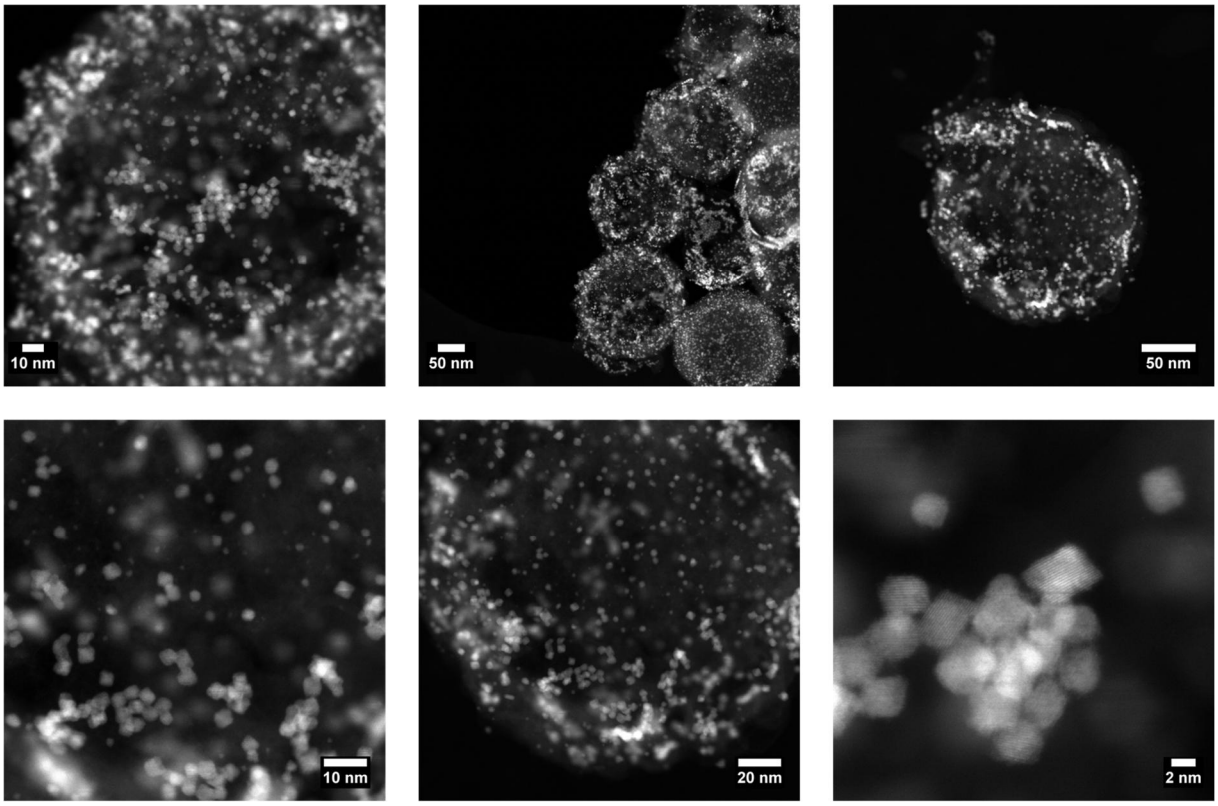

Figure S9: Dark field STEM images of Pt_{seed}/Pt_3Ni-Mo supported on HGS

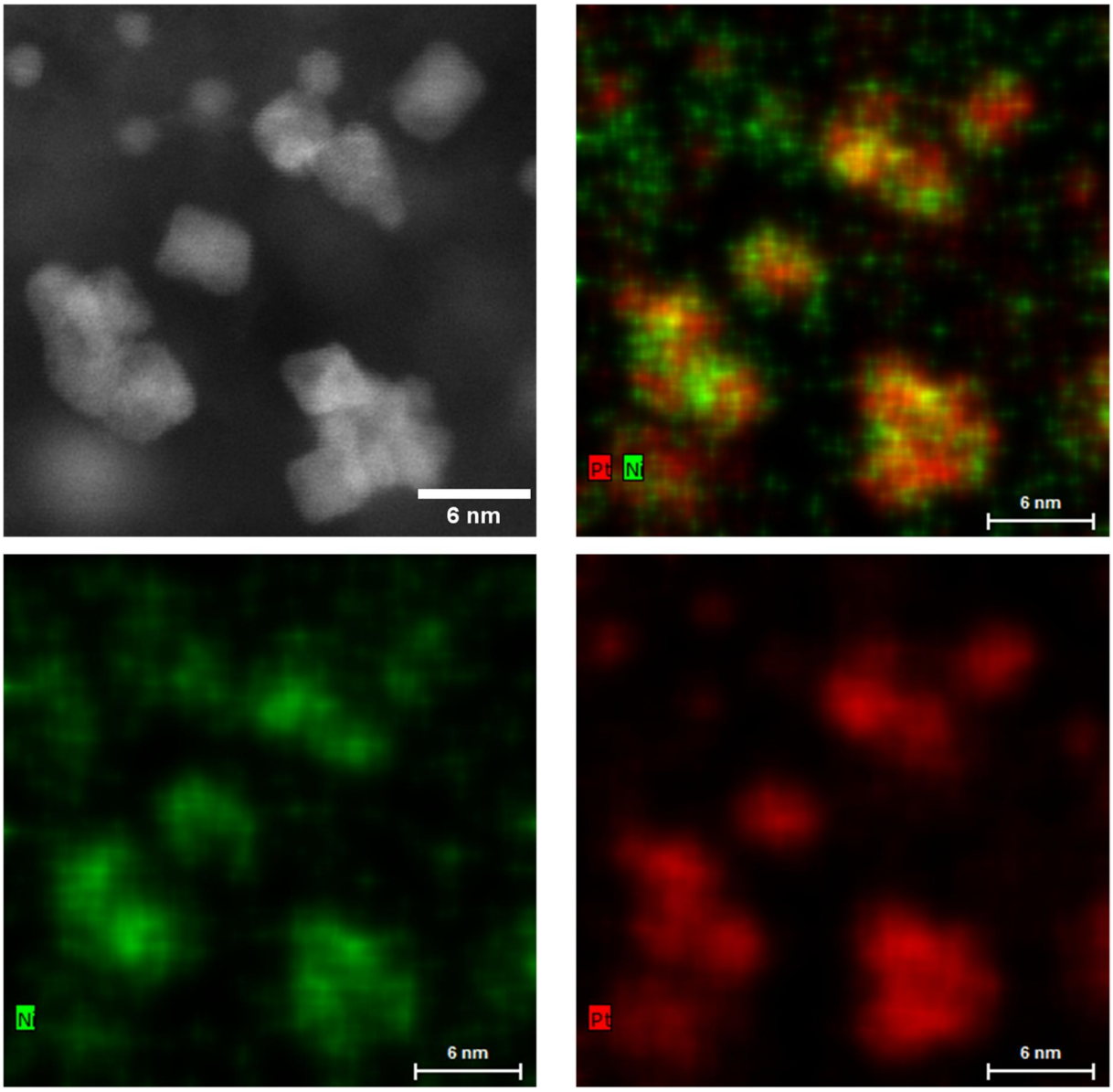

Figure S10: HAADF STEM micrographs of Pt_{seed}/Pt_3Ni-Mo/HGS and the corresponding EDX of the respective elements Pt and Ni.

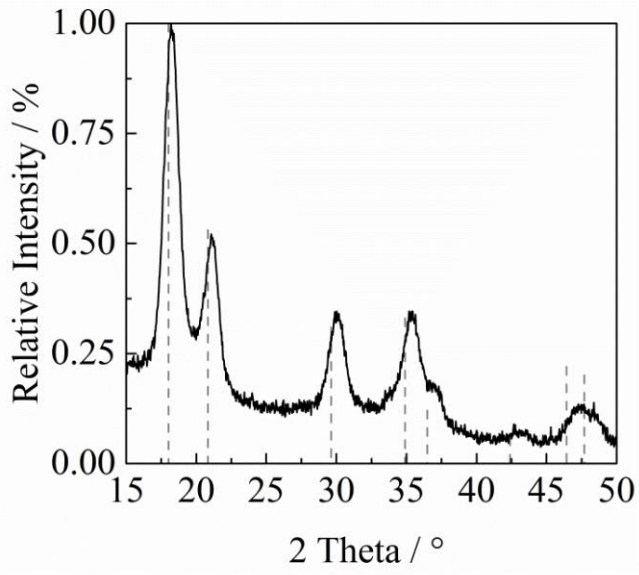

Figure S11: X-ray diffractogram of Pt_{seed}/Pt_3Ni-Mo/HGS. The grey dashed lines indicate the Pt reference [ICDD: 04-0802].

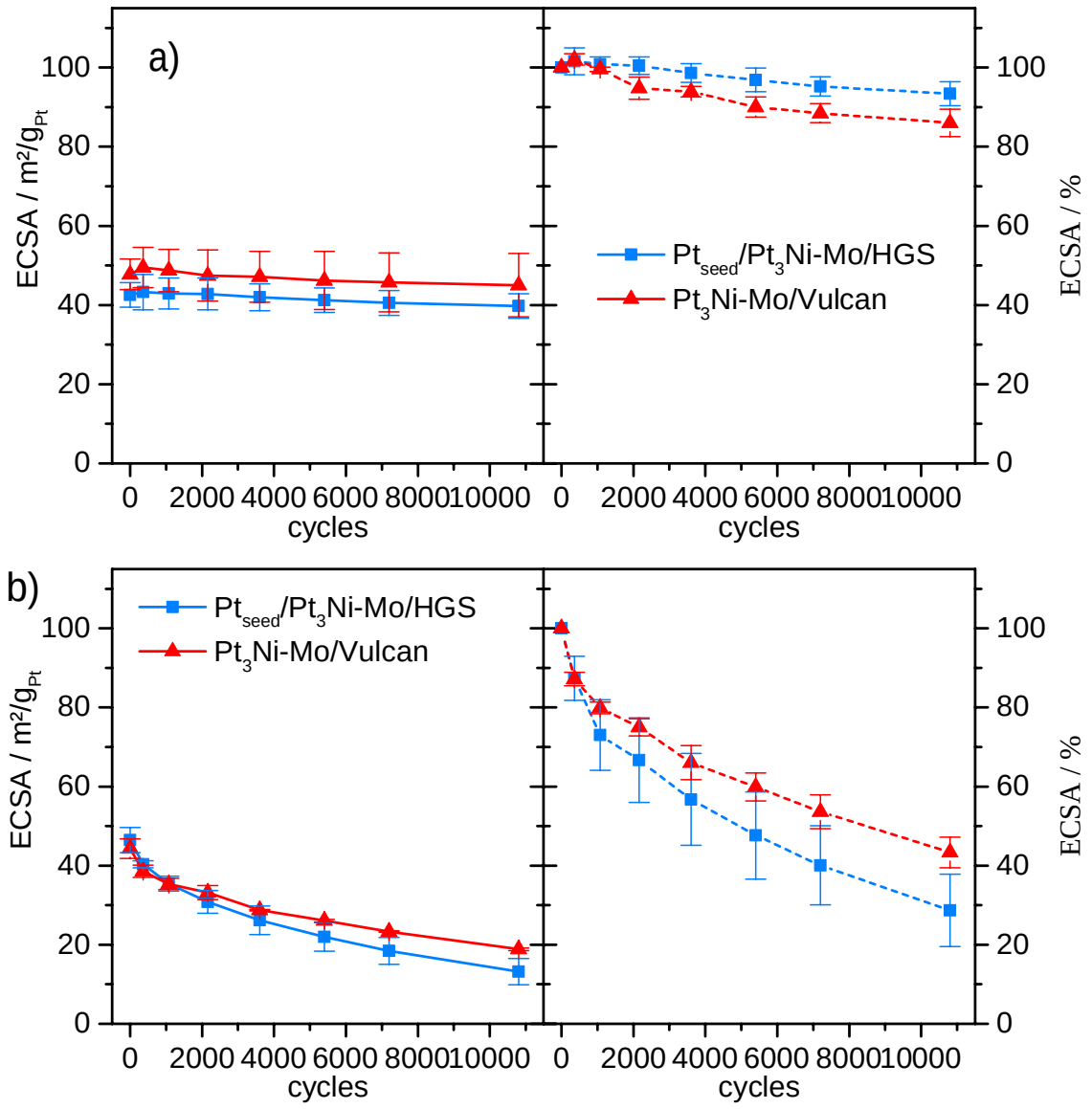

Figure S12: ECSA development (absolute and %) after different cycles and upper potential limits (a) ATS-1.0; b) ATS-1.4)

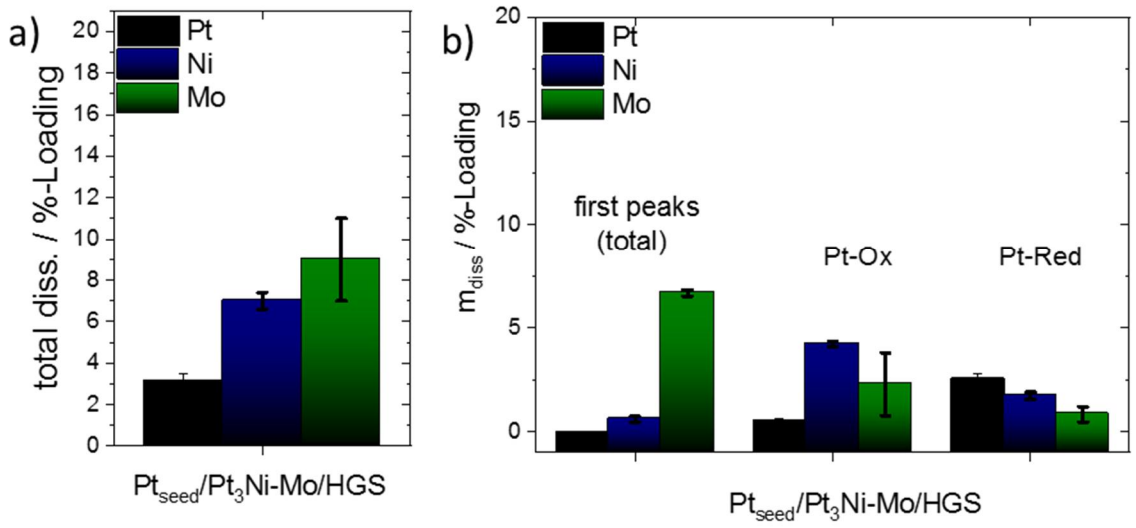

Figure S13: Quantification of ICP-MS results shown in Figure 5 (main manuscript) for Pt_{seed}/Pt_3Ni-Mo on HGS. a) Total dissolution during one potential cycling between 0 – 1.5 V_{RHE} in 0.1M $HClO_4$ without taking the contact dissolution peak into account. b) Specified quantification of the observed peaks. For simplification, the dissolution of Mo and Ni before Platinum oxidation (<1.0V vs. RHE) are combined and are named "first peaks (total)". The dissolution associated with Platinum oxidation is termed "Pt-Ox" while the dissolution associated with Platinum reduction is termed "Pt-Red".

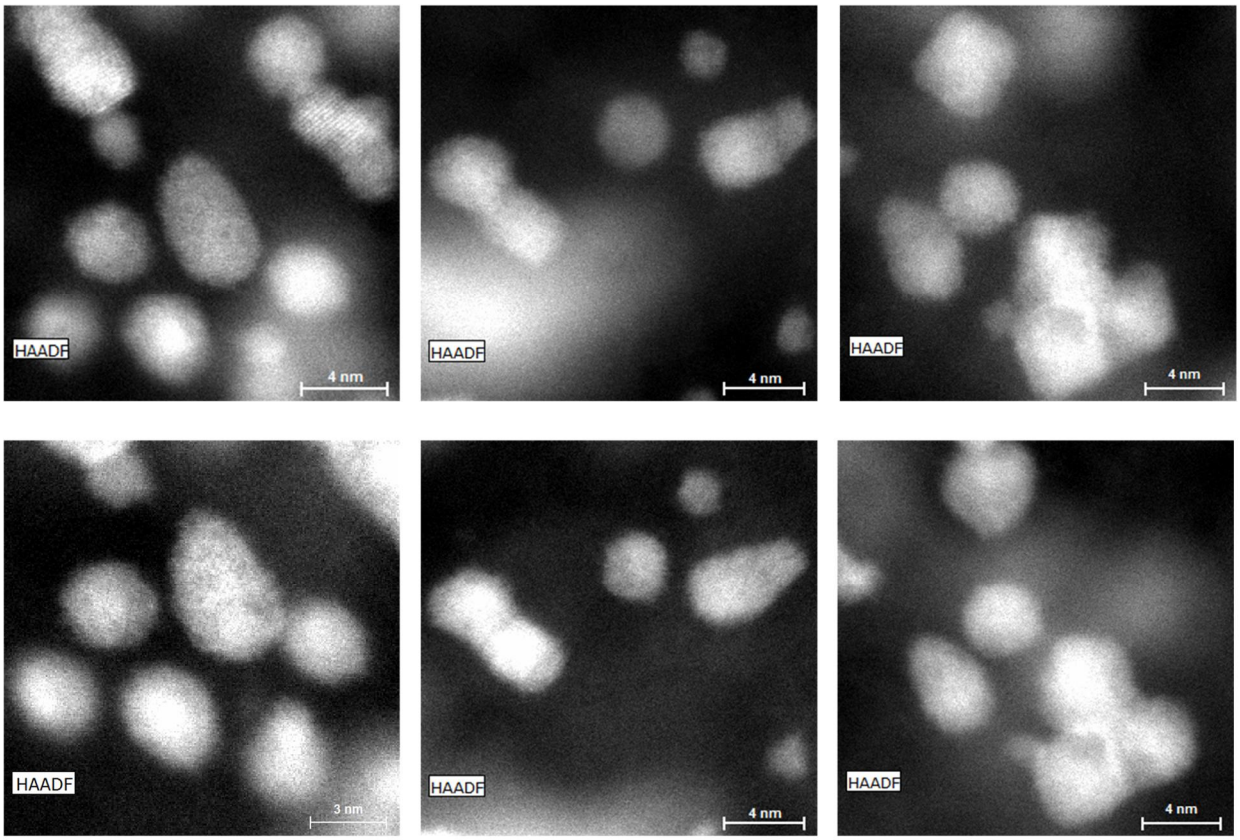

Figure S14: IL-TEM images of Pt_{seed}/Pt_3Ni-Mo/HGS before (top) and after 10800 potential cycling (bottom) between 0.4 and 1.0 V vs. RHE; 1 V s^{-1} in 0.1M $HClO_4$.

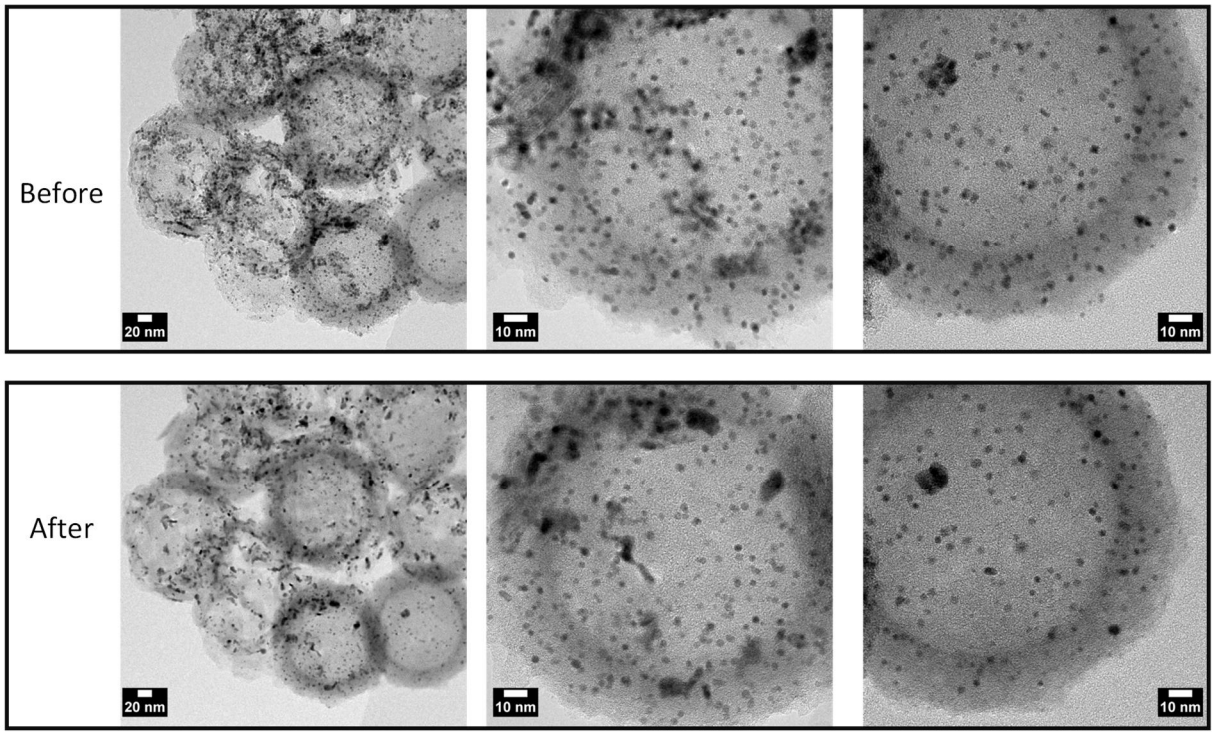

Figure S15: IL-TEM images of Pt_{seed}/Pt_3Ni-Mo/HGS before (top) and after 1000 potential cycling (bottom) between 0.4 and 1.4 V vs. RHE; 1 V s^{-1} in 0.1M $HClO_4$.

SFC-ICPMS experiments:

Method:

A SFC coupled to an ICP-MS (ICP-MS, NexION 300X, Perkin Elmer) was used to monitor dissolution processes in 0.1 M HClO (from ultrapure water (PureLab Plus system, Elga, 18 MΩ cm^{-1}, TOC < 3 ppb)) and concentrated $HClO_4$, (Merck, Suprapure®)).[4] The SFC was homemade out of polycarbonate with a working electrode opening of 0.035 cm^2. As counter electrode, a graphite rod was used. An Ag/AgCl (Metrohm, Germany) served as reference electrode. The reversible hydrogen electrode potential was determined prior to each measurement using a sputtered Pt-film and H_2 saturated 0.1M $HClO_4$. The potential was monitored at OCP for 30 minutes and the set-in potential from the last minute was used as RHE potential. A flow rate of 188 µL/min was adjusted while the electrolyte was purged with Argon. Each measurement day, a daily performance test was conducted for the ICP-MS in order to ensure proper working conditions. A four-point calibration was done before starting the measurements (usually in the morning). ^{103}Rh (for ^{98}Mo), ^{187}Re (^{195}Pt) and ^{74}Ge (^{60}Ni) was used as internal standard.

Peak assignment

For Pt, the expected transient oxide formation peaks (Pt-1) and reduction peaks (Pt-2) can be observed. The interested reader is referred to [5] for further detailed information. For Ni, an initial contact peak was observed. When the potential cycling starts at low potential, dissolution of Ni (Ni1) at relevantly low potentials (peak maximum: 0.1 V) was observed. We attribute this dissolution to nickel oxidation in agreement with thermodynamics (Pourbaix's diagram).[6] After dissolution of non-stabilized nickel, no nickel dissolution was observed until ca. 1.0 V. The following dissolution (Ni-2) goes along with Pt oxidation where the protecting Pt-shell dissolves partly, paving the way for dissolution of the underlying Ni. When cycling back, the dissolution drops to almost zero until dissolution starts again. The peak maximum of the third Ni-dissolution (Ni-3) coincides with the Pt-reduction dissolution. For

Mo, a similar trend was observed. Presumably, the first Mo dissolution peak (Mo-1) corresponds to Mo oxidation to Mo^{3+} followed by the oxidation to higher oxidation states (Mo-2). At this point, most of Mo is already dissolved from the octahedrally shaped nanoparticles. Therefore, only small Mo dissolution peaks due to Pt-oxidation (Mo-3) and reduction (Mo-4) were observed.

Rotating disk electrode measurements:

As potentiostat, a Gamry reference 600 was used. As working electrode, a home-made thin film rotating disk electrode was used. The glassy carbon disk embedded into the Teflon inlet was polished with alumina in water with particle sizes of 1 µm and 0.3 µm. The same Ag/AgCl reference electrode as in SFC experiments was used. A graphite rod served as counter electrode. For the determination of the electrocatalytically active surface area (ECSA), CO stripping was employed. The charge density was determined and divided by the charge density of bulk Pt (195 µC/cm^2). The obtained roughness factor was divided by the amount of catalyst deposited on the electrode. The resulting ESCA was used for the evaluation of specific (SA) and mass activity (MA). The SA was determined at 1600 rpm in oxygen saturated solution at 0.9 V vs. RHE (scan rate: 50 mV/s) as shown exemplarily in Figure S16. The capacitive response in Ar-saturated solution with the same scan rate and same potential window was subtracted. Exemplarily, Figure S16 shows ORR curves at different rotations speeds (400, 900, 1600 and 2500 rpm) at room temperature in O_2 saturated 0.1 M $HClO_4$. No activation treatment was performed beforehand in order not to alter the surface of the octahedrons. The lower ECSA of Pt_{seed}/Pt_3Ni(-Mo)/HGS is attributed to the larger particle dimensions (ca. 4 nm) compared to Pt/C (ca. 3 nm). Similar to SFC experiments, the RHE potential was determined before each measurement in hydrogen saturated solution with a Pt-sputtered film. The stability was evaluated by accelerated degradation protocols cycling the WE from 0.4 V to either 1.0 V (AST-1.0) or 1.4 V (AST-1.4) for 10800 times. After 0, 360, 1080, 2160, 3600, 5400, 7200 and 10800 potential cycles, the ECSA was monitored through CO stripping as shown exemplarily in Figure S16. Similar to activity measurements, the capacitive responses were subtracted by recording current voltage curves in Argon saturated solution. Additional information can be found in [23].

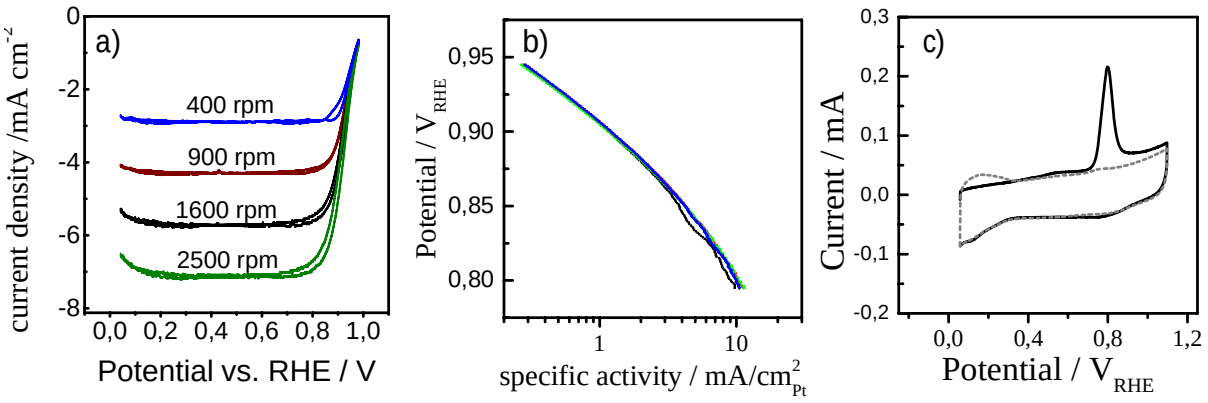

Figure S16: Exemplary cyclic voltammogram of Pt_{seed}/Pt_3Ni-Mo/HGS at different rotation rates (400, 900, 1600, 2500) in oxygen saturated 0.1 M $HClO_4$ (scan rate 0.05 V s-1) after subtraction of capacitive background currents. b) the corresponding Tafel plots. c) CO stripping after CO adsorption (straight line) and purging with Ar and only in Ar (dashed) saturated 0.1M $HClO_4$.

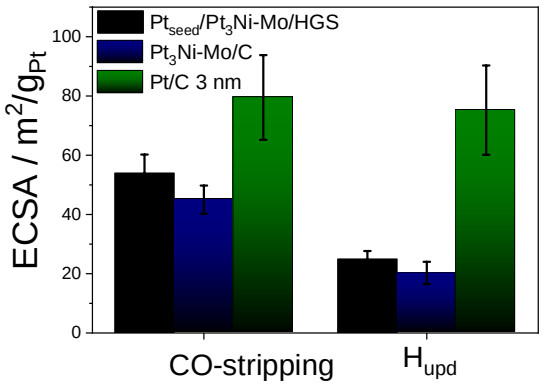

Figure S17: Comparison between CO-stripping and H_{UPD} for Pt_{seed}/Pt_3Ni-Mo/HGS, Pt_3Ni-Mo/C and Pt/C (3 nm, TKK).

Electron microscopy:

For the IL-STEM experiments, gold TEM finder grids (S147A9, Plano GmbH) were coated with an aqueous catalyst suspension (10 mL, 0.05 g_{cat} L^{-1}). After drying, the sample was examined in a C_s-corrected (CEOS GmbH) FEI Titan 80-200 ("ChemiSTEM") electron microscope equipped with a high angle annular dark field (HAADF) detector. "Z-contrast" conditions were achieved by using a probe semi-convergence angle of 24.7 mrad and an inner collection semi angle of 88.4 mrad. The microscope was operated at 80 kV to minimize beam damage. Elemental maps were recorded by EDX using four large-solid-angle symmetrical Si drift detectors. For the quantification, Pt_L Ni_K edges were used. For each material, 15 HAADF STEM images and corresponding elemental maps of different catalyst agglomerates were acquired. To exclude beam damage, the acquisition time for each map was 5 min. Afterwards, the catalyst covered TEM grid was used as a working electrode in electrochemical degradation experiments and a carbon rod acted as counter electrode. For the accelerated aging experiments, the potential was cycled between 0.4 and 1 V *vs.* RHE for 10800 times with a potentiostat (SP 50, Bio-Logic Science Instruments) at 20°C. The homemade three electrode glass cell was equipped with a RHE as reference electrode (Gaskatel HydroFlex). Argon saturated perchloric acid (0.1 mol L^{-1}, Merck, suprapur) was used as electrolyte. The iR drop was measured and was corrected for by the current interrupt method. After the AST, the grid was dipped several times into ultrapure water to remove electrolyte residues. After drying, the grid was transferred to the electron microscope and the pre-characterized catalyst agglomerates were reexamined.

Microtome sectioning

The powdered sample was embedded in a low viscosity resin and thin microtome sections (~50 nm) were prepared using a Reichert Ultracut microtome.

Nitrogen-physisorption

Micromeritics 3 Flex and ASAP 2010 instrument were used for measuring N2-sorption. Prior to the analysis, the powder materials were activated under vacuum for > 8 h at 250 °C. For N_2-physisorption experiments, a static volumetric method at 77.4 K was used with a relative pressure tolerance of 5% for the equilibration intervals. The adsorption branch in the range of 0.05 to 0.25 p/p_0 was used for BET surface area calculations. The pore size distribution was obtained using the desorption branch by applying the Barrett, Joyner and Halenda (BJH) method. In case of pores in the range of 3 to 5 nm, the adsorption branch is applied for the pore size distribution due to artifacts i.e. forced closure, cavitation or pore-blocking. For the desorption scanning, multiple individual measurements cycles of the

hysteresis were applied, since total measurement time exceeded the time given by the liquid nitrogen for cooling.

Quantification of the change in octahedral geometry:

The change of the octahedra geometry was analysed to estimate the loss of the highly active 111 surface. The 2D projection of particles in or close to the 110 zone axis resemble a rhombus and the longest diagonal corresponds to the total height/length of an octahedron h. The change of h was determined by measuring the respective length at identical locations before (h) the AST-1.0 and thereafter (h_{ast}) and the length changes h_p was determined by subtraction.

As a result of the accelerated stress test, 6% of the particles showed a positive relative contraction. The average value of contraction is 15%. The measured average contraction of the octahedra is connected to a loss of their {111} facets and a shape change towards a more spherical shape. Due to the accelerated stress test, 10% of the octahedra aligned in the 110 zone axis change their morphology to spherical particles. All of the observed particles aligned in the 110 zone axis showed an increase in the deterioration of the edges resulting in the formation of truncated octahedra.

In the following, a rough estimate of the change in the {111} surface area is performed. We approximated the shape change from an idealized perfect octahedron to a truncated octahedron, with the loss at the edges being approximated by equilateral square pyramids with height h_p.

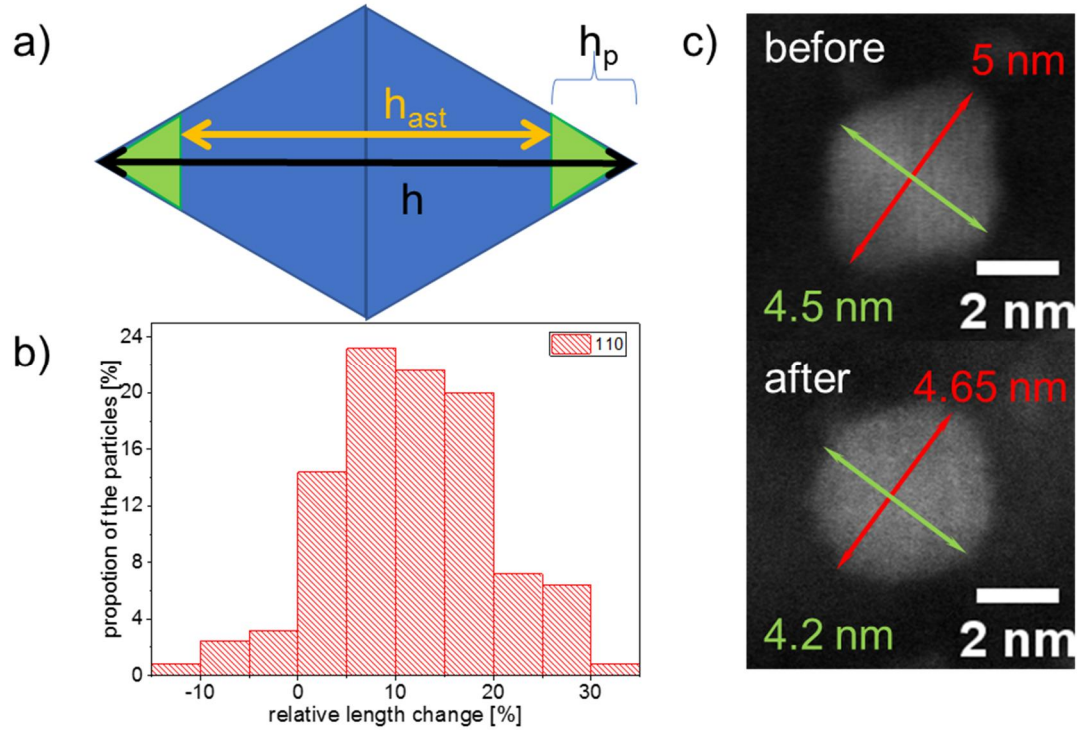

Figure S18: a) Schematic representation of an octahedron aligned in the 110 zone axis. b) Histogram of the relative length changes caused by AST-1.0. For this investigation, 125 octahedra aligned in the 110 zone axis were analysed at identical locations before and after AST-1.0. C) Representative HAADF-STEM image of an octahedron aligned in the 110 zone axis before and after the AST.

The average length contraction of 15 % results in the total loss of the 111 surface of 9% ± 6.3%, assuming that each corner has the same degradation rate. As this approximation assumes the formation of perfectly facetted truncated octahedra, the real loss of {111} facets is most probably underestimated, as the particles show a clear rounding at the corners after AST.

References:

(1) Galeano, C.; Meier, J. C.; Peinecke, V.; Bongard, H.; Katsounaros, I.; Topalov, A. A.; Lu, A. H.; Mayrhofer, K. J. J.; Schuth, F. *Toward Highly Stable Electrocatalysts via Nanoparticle Pore Confinement*; *Journal of the American Chemical Society* 2012, *134*, 20457.
(2) Baldizzone, C.; Mezzavilla, S.; Carvalho, H. W. P.; Meier, J. C.; Schuppert, A. K.; Heggen, M.; Galeano, C.; Grunwaldt, J. D.; Schuth, F.; Mayrhofer, K. J. J. *Confined-Space Alloying of Nanoparticles for the Synthesis of Efficient PtNi Fuel-Cell Catalysts*; *Angewandte Chemie-International Edition* 2014, *53*, 14250.
(3) Büchel, G.; Unger, K. K.; Matsumoto, A.; Tsutsumi, K. *A Novel Pathway for Synthesis of Submicrometer-Size Solid Core/Mesoporous Shell Silica Spheres*; *Advanced Materials* 1998, *10*, 1036.
(4) Klemm, S. O.; Karschin, A.; Schuppert, A. K.; Topalov, A. A.; Mingers, A. M.; Katsounaros, I.; Mayrhofer, K. J. J. *Time and potential resolved dissolution analysis of rhodium using a microelectrochemical flow cell coupled to an ICP-MS*; *Journal of Electroanalytical Chemistry* 2012, *677–680*, 50.
(5) Topalov, A. A.; Katsounaros, I.; Auinger, M.; Cherevko, S.; Meier, J. C.; Klemm, S. O.; Mayrhofer, K. J. J. *Dissolution of Platinum: Limits for the Deployment of Electrochemical Energy Conversion?*; *Angewandte Chemie-International Edition* 2012, *51*, 12613.
(6) Pourbaix, M. *Atlas of electrochemical equilibria in aqueous solutions*; National Association of Corrosion Engineers, 1974.